

1           **PV power modelling using solar radiation from ground-based**  
2           **measurements and CAMS: Assessing the diffuse component related**  
3           **uncertainties leveraging the Global Solar Energy Estimator (GSEE)**

4           Nikolaos Papadimitriou<sup>1,2</sup>, Ilias Fountoulakis<sup>2</sup>, Antonis Gkikas<sup>2</sup>, Kyriakoula  
5           Papachristopoulou<sup>3</sup>, Andreas Kazantzidis<sup>1</sup>, Stelios Kazadzis<sup>3</sup>, Stefan Pfenninger<sup>4</sup>, John  
6           Kapsomenakis<sup>2</sup>, Kostas Eleftheratos<sup>5,6</sup>, Athanassios A. Argiriou<sup>1</sup>, Lionel Doppler<sup>7</sup>, and  
7           Christos S. Zerefos<sup>2,6,8,9</sup>

8           <sup>1</sup>Department of Physics, University of Patras, 26500 Patras, Greece

9           <sup>2</sup>Research Centre for Atmospheric Physics and Climatology, Academy of Athens, 11521 Athens,  
10           Greece

11           <sup>3</sup>Physikalisch-Meteorologisches Observatorium Davos, World Radiation Center (PMOD/WRC), 7260  
12           Davos, Switzerland

13           <sup>4</sup>Faculty of Technology, Policy, and Management (TPM), Delft University of Technology, 2628 BX  
14           Delft, the Netherlands

15           <sup>5</sup>Department of Geology and Geoenvironment, National and Kapodistrian University of Athens,  
16           15784 Athens, Greece

17           <sup>6</sup>Biomedical Research Foundation, Academy of Athens, 11527 Athens, Greece

18           <sup>7</sup>Deutscher Wetterdienst, Meteorologisches Observatorium Lindenberg – Richard Assman  
19           Observatorium (DWD, MOL-RAO), 15848 Lindenberg (Tauche), Germany

20           <sup>8</sup>Navarino Environmental Observatory (N.E.O.), 24001 Messinia, Greece

21           <sup>9</sup>Mariolopoulos-Kanaginis Foundation for the Environmental Sciences, 10675 Athens, Greece

22           Corresponding author: Nikolaos Papadimitriou ([npapadimitriou@academyofathens.gr](mailto:npapadimitriou@academyofathens.gr), Vasilissis  
23           Sofias 79, 11521 Athens, Greece)

24           **Abstract**

25           Accurate PV power production modelling requires precise knowledge of the distribution of solar  
26           irradiance among its direct and diffuse components. Since this information is rarely available, this

27 requirement can be addressed through the use of diffuse fraction models. In this study, we try to  
28 quantify the errors in PV modelling when measurements of the diffuse solar irradiance are not  
29 available. For this purpose, we use total and diffuse solar irradiance data obtained from ground-  
30 based measurements of BSRN to simulate the PV electric output using GSEE. We have chosen five  
31 sites in Europe and North Africa, with different prevailing conditions, where BSRN measurements are  
32 available. GSEE incorporates an implementation of the Boland-Ridley-Lauret (BRL) diffuse fraction  
33 model, along with a Climate Data Interface that enables simulations across different time scales.  
34 We evaluate the capability of BRL in providing accurate estimations of the diffuse fraction under  
35 diverse atmospheric conditions, with particular attention on the presence of clouds and aerosols  
36 and assess the extent to which its associated errors propagate to energy production modelling.  
37 Furthermore, we compare GSEE outputs when using CAMS radiation time-series as input instead of  
38 ground-based measurements, to quantify the impact of the CAMS radiation product uncertainties in  
39 PV modelling.

40 **Keywords**

41 Solar energy modelling; CAMS radiation; PV power modelling; aerosol; dust; solar radiation

42 **1. Introduction**

43 Decarbonizing the power sector in a sustainable manner is pivotal in the effort to mitigate climate  
44 change (Edenhofer et al., 2011; Owusu and Asumadu-Sarkodie, 2016; IPCC, 2022) and the large-  
45 scale deployment of Solar Energy offers significant prospects toward this objective (Kakran et al.,  
46 2024). The available solar energy is a variable source, fluctuating across different timescales with a  
47 unique solar-resource profile over individual locations (McMahan et al., 2013). Therefore, accurate  
48 solar energy forecasting and resource assessment is crucial for minimizing the risk in selecting  
49 project location, designing the appropriate solar-energy conversion technology, and integrating new  
50 sources of solar based power generation into the electricity grid (Stoffel, 2013), while short-term,  
51 intra-hour forecasts are critical for power plant operations, grid-balancing, real-time unit  
52 dispatching, automatic generation control, and trading (Pedro et al., 2017).

53 Extending solar irradiance forecasting to derive PV power forecasts is essential in solar energy  
54 applications. PV power modelling can be achieved through the following additional steps to solar  
55 irradiance forecasting: (i) decomposing Global Horizontal Irradiance (GHI) into Diffuse Horizontal  
56 Irradiance (DHI) and Direct Normal Irradiance (DNI); (ii) calculating the plane-of-array irradiance

57 incident on the surface of PV planes, whether static or mounted on a solar tracking system, and (iii)  
58 simulating the PV power production primarily based on the in-plane irradiance (Blanc et al., 2017).

59 The scarcity of concurrent measurements of both solar irradiance components, coupled with the  
60 complexity of their theoretical computation, has driven the development of numerous empirical  
61 models for estimating the diffuse fraction (ratio of the diffuse-to-global solar radiation). A seminal  
62 contribution in this area was made by Liu and Jordan (1960), who established a correlation between  
63 the diffuse fraction and the clearness or cloudiness index (ratio of the global-to-extraterrestrial  
64 radiation). These models predominantly rely on the clearness index as the principal predictor. They  
65 are generally classified into single-predictor models and multi-predictor models, with the latter  
66 incorporating additional astronomical variables for enhanced precision (Paulescu and Blaga, 2019).  
67 Typically, these models are expressed as polynomial equations, ranging from the 1<sup>st</sup> to the 4<sup>th</sup> degree,  
68 that link the diffuse fraction to the clearness index  $DF = f(\text{clearness index, } * \text{params})$  (Jacovides  
69 et al., 2006). Boland et al. (2001) proposed the use of a logistic function instead of linear or simple  
70 nonlinear functions of the clearness index. Ridley et al. (2010) developed a multiple-predictor  
71 logistic model, known as the Boland-Ridley-Lauret (BRL), which combines simplicity and reliable  
72 performance across both the Northern and Southern Hemispheres. The BRL model extends Boland's  
73 approach by adopting the hourly clearness index as the principal predictor and introducing the  
74 following additional parameters: apparent solar time, daily clearness index, solar altitude, and a  
75 measure of the persistence of global radiation level. In the implementation of the BRL included in  
76 the GSEE, the users set as input only the hourly clearness. Moreover, this implementation adopts the  
77 updated parameters proposed by Lauret et al. (2013), which derived using data from nine worldwide  
78 locations covering a variety of climates and environments across Europe, Africa, Australia and Asia.  
79 While the existing models consider all-sky conditions, in solar energy modelling it is critical to focus  
80 on cloud-free skies, where energy production is maximized. Under such conditions, aerosols  
81 become the primary parameter influencing the distribution of solar irradiance among its  
82 components. (e.g., Blaga et al., 2024). Specifically, the BRL model accounts for aerosols indirectly  
83 through the clearness index, which is indicative of the overall atmospheric attenuation of solar  
84 radiation.

85 In regions dominated by abundant sunshine, such as the Mediterranean and Middle East, which are  
86 favorable for solar based power generation, the attenuation of solar irradiance is strongly influenced  
87 by aerosols, and particularly desert dust aerosols. Several studies highlighted the impact of desert

88 dust aerosol in the downwelling solar irradiance and the energy production in these regions  
89 (Fountoulakis et al., 2021; Papachristopoulou et al., 2022; Kosmopoulos et al., 2018; Kouklaki et al.,  
90 2023). The significance of considering the effect of aerosols in short-term solar irradiance forecasting  
91 and nowcasting is emphasized by Kazantzidis et al. (2017), Raptis et al. (2023) and  
92 Papachristopoulou et al. (2024).

93 The Global Solar Energy Estimator (GSEE; Pfenninger and Staffell, 2016) is a widely used open access  
94 model for simulating PV power output, designed for rapid calculations and ease of use. It comes with  
95 an implementation of the BRL diffuse fraction model (Ridley et al., 2010; Lauret et al., 2013).

96 While PV power modelling is essential for linking solar resources to energy production, the existing  
97 literature does not adequately address its reliability under diverse atmospheric conditions. To the  
98 best of our knowledge, the existing literature does not include studies that explicitly address the  
99 uncertainties in PV energy production modeling associated with the partitioning of solar radiation  
100 into its direct and diffuse components at the model input. In this study, we supply GSEE with input  
101 data from ground-based measurements as well as from the Copernicus Atmospheric Monitoring  
102 Service (CAMS), aiming to investigate differences in PV power output simulations, which arise from  
103 providing only GHI as input radiation data. At the outset, we focus on evaluating the reliability of BRL  
104 under diverse atmospheric conditions, with particular attention to the dependence of its accuracy  
105 on the presence of clouds and aerosols. To further explore this, we conduct a sensitivity analysis  
106 using radiative transfer model (RTM) simulations under cloud-free skies. Following these analyses,  
107 we assess the extent to which the associated uncertainties in the estimation of the diffuse fraction  
108 spread to the power generation over hourly intervals. This step involves simulating PV plants with  
109 varying configurations. GSEE is also effective for analyzing trends and variability in solar based power  
110 generation through its climate interface submodule (e.g., Hou et al., 2021), where the BRL model is  
111 integrated within the internal processing chain. The accuracy of the climate interface in estimating  
112 the total daily PV power output is also evaluated in this study.

113

## 114 **2. Data and Methodology**

### 115 2.1 Global Solar Energy Estimator (GSEE)

116 The modelling of the PV power output is conducted using the version 0.3.1 of GSEE (Pfenninger and  
117 Staffell, 2016). The model features functions for simulating a complete PV system, incorporating

118 characteristics and specifications such as location, installed capacity, technology, tracking (fixed, 1-  
119 axis, 2-axis), tilt angle, and orientation.

120 The user provides as input time-series data of solar radiation, and optionally, ambient air  
121 temperature and surface albedo. Specifically, the model requires GHI and, when available, the  
122 Diffuse Fraction. If the diffuse component is not provided, the provided implementation of the BRL  
123 diffuse fraction model (Ridley et al., 2010; Lauret et al., 2013) is employed to estimate it, relying only  
124 on time-series of the hourly clearness index and the geographical coordinates. While in the single-  
125 site application of the GSEE model with hourly time resolution the user has the option to adjust the  
126 input and select alternative diffuse fraction models implemented by external libraries, e.g., pvlib  
127 (Anderson et al., 2023), the climate data interface automatically invokes the BRL model as part of the  
128 internal processing workflow. GSEE utilizes the provided information for the distribution of the  
129 irradiance components and applies trigonometric calculations to determine the total solar  
130 irradiance incident on the panel's inclined plane. More precisely, for the plane-of -array irradiance  
131 calculation a GSEE includes the submodule "trigon" (transposition model), which is based on  
132 trigonometric formulations, that account of the surface albedo, thereby including the ground-  
133 reflected component of solar radiation. However, the transposition model is integrated within the  
134 GSEE internal algorithms, so it cannot be modified by the user.

135 After solar irradiance the most significant parameter regarding energy production is air temperature  
136 (e.g., Dubey et al., 2013). If temperature is not provided by the user, the model assumes a default  
137 value of 20 °C. In this study, temperature was used as input only in the simulations with BSRN data,  
138 as it is provided alongside radiation measurements. A surface albedo value of 0.3 considered by  
139 default from the model, introduces some uncertainty in our simulations, which however is estimated  
140 to be small. Under cloudless conditions, a 10% difference in surface albedo changes the GHI by ~1%  
141 for  $SZA < 75^\circ$ . Differences are larger under cloudy conditions (~ 10% difference in GHI for a 10%  
142 difference in surface albedo). Nevertheless, surface albedo at the selected sites is generally low and  
143 relatively invariant throughout the year (even at the most northern site of Lindenberg there is only a  
144 limited number of days with increased surface albedo due to snow cover).

145 The available options for the panel type are crystalline silicon (c-Si) and Cadmium Telluride (CdTe),  
146 where the power output is modeled based on the relative PV performance model described by Huld  
147 et al. (2010). For fixed panels, a built-in latitude dependent function for the optimal tilt is also  
148 included.

149 Moreover, GSEE includes a Climate Data Interface submodule that enables the processing of gridded  
150 climate datasets, with varying temporal resolutions, ranging from hourly to annual. Within the  
151 context of this submodule, the use of BRL serves as part of the resampling and upsampling  
152 processes applied to input climate datasets with daily resolution. For processing data with lower-  
153 than-daily resolutions, it incorporates the use of Probability Density Functions (PDFs), which  
154 describe the probability with which a day with a certain amount of radiation occurs within a month  
155 (GSEE, 2026). This methodology accounts for the non-linear distribution of mean monthly radiation  
156 across individual days, ensuring a more representative temporal disaggregation. The processes  
157 applied to the mean daily irradiance are described in detail in Section 3.4.

158 For the purposes of this study, we simulated solar plants with capacity of 1 kWp, and for both  
159 available technologies. The simulations with c-Si technology, considered as default by the model,  
160 are presented in detail the following sections. The results of the simulations with CdTe technology  
161 are provided in the supplement, and are not thoroughly discussed, since they are very similar to the  
162 results for the c-Si technology. Regarding the mounting approach, the solar plants were either static  
163 and oriented to the south or equipped with a 2-axis solar tracking system. In the case of fixed panels,  
164 we selected the optimal tilt angle relying on the latitude dependent built-in function.

165 The input parameters defining the characteristics of the simulated PV plants are summarized in Table  
166 1.

167 **Table 1.** Input parameters defining the characteristics of the simulated PV plants

Capacity	Mounting Approach			Technology	
1 kWp	Fixed		2-axis tracking	c-Si	CdTe
	Orientation: south	Tilt Angle: $f(\text{latitude})$ built-in function for optimal tilt			

168

169 2.2 Ground-based measurements

170 We supplied GSEE with ground-based irradiance as well as ambient temperature measurements  
171 collected from five stations of the Baseline Surface Radiation Network (BSRN; Driemel et al., 2018).  
172 Moreover, information about aerosols was retrieved from co-located stations of the Aerosol Robotic  
173 Network (AERONET; Holben et al., 1998; Dubovik et al., 2000).

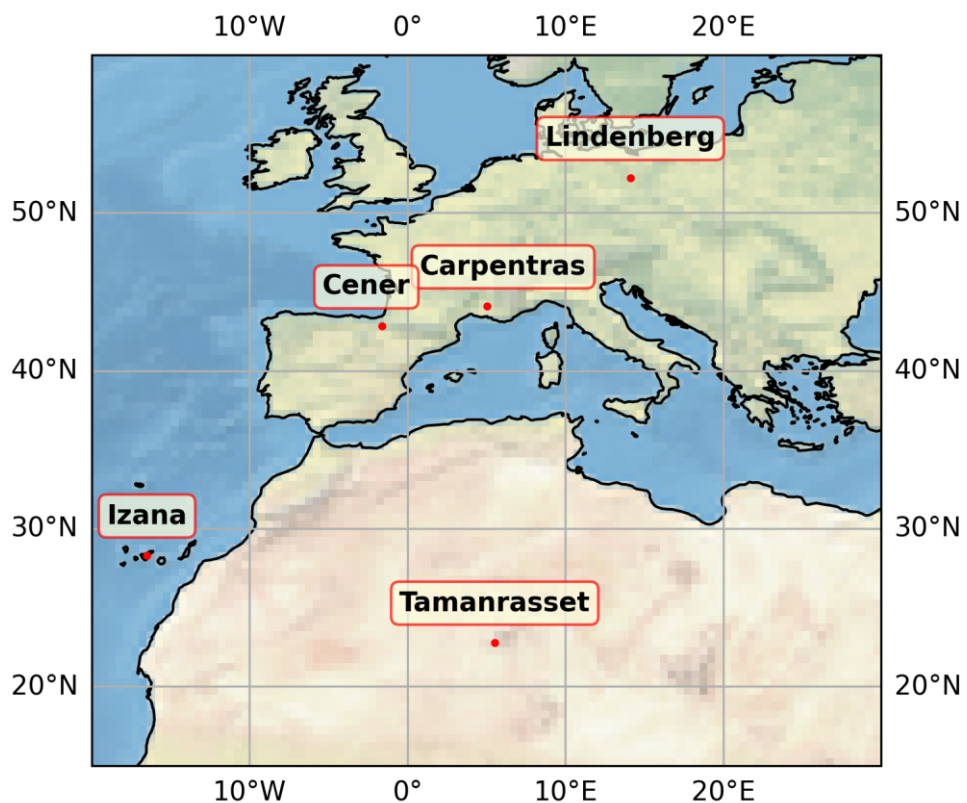
174 Information for the stations utilized for this study is summarized in Table 2, and their geographical  
175 location is depicted in Figure 1.

176

177 **Table 2.** Detailed information about the location of the ground-based stations used in this study.

STATION	Latitude [° N]	Longitude [° E]	Elevation [m]
Carpentras (CAR)	44.08	5.06	100
Cener (CNR)	42.82	-1.60	471
Izaña (IZA)	28.31	-16.50	2373
Lindenberg (LIN)	52.21	14.12	125
Tamanrasset (TAM)	22.79	5.53	1385

178



179

180      **Figure 1.** Locations of the BSRN and co-located AERONET stations that are used in the current  
181      study

182

183      BSRN station-to-archive files were accessed and manipulated using the SolarData v1.1 R package  
184      (Yang, 2019), and the BSRN-recommended quality check (QC) tests (Long and Dutton, 2010) applied  
185      to the collected data. Some data gaps arose due to measurements removed during the QC  
186      procedure. Although these data gaps are, in most cases, shorter than 2-3 hours, they may affect the  
187      BRL performance throughout the corresponding days. Consequently, days affected by such data  
188      gaps excluded from the analysis. We retrieved data for 2017, with 1-minute temporal resolution. We  
189      used GHI, DHI, and Temperature as inputs to the GSEE model. Initially, the data were resampled to  
190      hourly and mean hourly values of GHI and DHI are calculated. Then, the simulations were conducted  
191      using either GHI and DHI, or only GHI along with the deployment of BRL. The input to BRL consists of  
192      hourly clearness index, derived by dividing GHI measurements with the solar radiation incident on a  
193      horizontal plane at the Top of the Atmosphere (TOA) above the examined location. Subsequently, the  
194      1-min timeseries resampled also to a daily resolution and transformed into three-dimensional  
195      arrays,  $GHI = f(\text{time}, \text{lat}, \text{lon})$ , where the spatial dimensions of each dataset corresponded to a  
196      unique point defined by the coordinates of the associated station. Simulations with the daily time-  
197      resolved dataset were performed using the Climate Data Interface.

198      Representing cloudiness is a challenging task that requires several observations. For this purpose,  
199      aiming to obtain an indicative measure of the intra-hour cloudiness conditions we adopted the  
200      following formulation. Specifically, measurements of Direct Normal Irradiance (DNI) were utilized to  
201      obtain information for cloudiness relying on the conditions stated by WMO (2021), according to  
202      which sunshine duration is the total period where DNI exceeds  $120 \text{ W/m}^2$ . Alternative approaches  
203      such as the Cloud Modification Factor, require estimates of the clear sky irradiance, which  
204      introduces additional uncertainty. For the purpose of this analysis, we introduced a solar visibility  
205      (SV) parameter. Specifically, we assigned the value 0 when sun was obscured and the value 1 when  
206      visible. Aiming to describe the mean intra-hour cloudiness conditions, we considered the sky as  
207      cloud-free, cloudy, and partly cloudy based on the mean SV for the entire corresponding hour as  
208      follows:

$$\langle SV \rangle_{hour}: \begin{cases} 1 & \text{cloud-free} \\ \in (0,1) & \text{partly cloudy} \\ 0 & \text{cloudy} \end{cases}$$

210 For aerosol information, we accessed the AERONET Version 3 (V3) (Giles et al., 2019) and retrieved  
 211 level 2.0 data (from direct sun measurements) for Aerosol Optical Depth at 500nm ( $AOD_{500}$ ), which  
 212 serves as a representative measure of the aerosol load; Ångström Exponent between 440 and 870  
 213 nm wavelengths ( $AE_{440-870}$ ), where values near 0 correspond to coarse dust particles and values  
 214 around 2 to fine (e.g., smoke) particles (Dubovik et al., 2002); and Fine Mode Fraction at 500nm  
 215 ( $FMF_{500}$ ) obtained from the Spectral Deconvolution Algorithm (SDA) retrievals, to distinguish aerosol  
 216 into fine and coarse mode. The data were resampled at hourly intervals and a mean hourly value  
 217 calculated. After, the hourly mean values divided into clusters based on  $AOD_{500}$ , reflecting different  
 218 levels of aerosol load and allowing us to quantify their impact on solar energy production. To  
 219 investigate the impact related exclusively to aerosols, we included only hours with cloud-free sky  
 220 conditions. The clusters are defined in detail as follows:

- 221 •  $AOD_{500} \leq 0.05$ : Low aerosol load
- 222 •  $0.05 < AOD_{500} \leq 0.15$ : Moderate aerosol load
- 223 •  $0.15 < AOD_{500} \leq 0.3$ : High aerosol load
- 224 •  $AOD_{500} > 0.3$ : Very high aerosol load

225 To evaluate the performance of the Climate Interface over daily intervals, we defined the sunny  
 226 (cloudless) days using the condition:  $\langle SV \rangle_{day} \geq 0.9$ . Next, to characterize the average aerosol  
 227 conditions on sunny days, we applied the following classification:

- 228 •  $\langle AOD_{500} \rangle_{day} \leq 0.05$ : very-low aerosol
- 229 •  $\langle AOD_{500} \rangle_{day} > 0.05$ : aerosol-laden

230 Detailed comparisons of the energy production over hourly and daily integrals under the various  
 231 predefined sky conditions are provided in the supplement through evaluation metrics.

232 The selected locations have quite different atmospheric conditions regarding cloudiness and  
 233 aerosols. Additionally, they vary in altitude. A brief overview of the prevailing conditions derived from  
 234 the ground-based data is provided on the supplement. Regarding cloudiness, it is notable that in  
 235 Lindenberg the sky is generally overcast, whereas in southern locations sunshine dominates. In  
 236 terms of aerosols, very high aerosol loads occur more frequently in Tamanrasset. As for aerosol type,

237 there is considerable variation among the examined locations: Carpentras, Cener, and Lindenberg  
238 are primarily influenced by fine mode aerosols, while Tamanrasset and Izaña are mostly affected by  
239 coarse mode aerosols.

240 For investigating the impact of desert dust aerosol in solar based power generation, Tamanrasset  
241 serves as a representative and exceptional case because it is in a region with important sources of  
242 Saharan dust aerosols (Faid et al., 2012). Meanwhile, Izaña, located in subtropical North Atlantic, is  
243 a high mountain station within the free troposphere, affected mineral dust when the Saharan Air  
244 Layer top exceeds the station height, especially through August to October (Toledano et al., 2018;  
245 Cuevas et al., 2019). Due to its high altitude, Izaña avoids contamination from local or regional  
246 sources (Barreto et al. 2022). The Canary Islands, where Izaña is located, are influenced by extreme  
247 dust events that cause a significant decrease in PV power generation (Canadillas-Ramallo et al.,  
248 2022). In South Europe, which is also affected by the transport of Saharan dust across the  
249 Mediterranean, aerosol types exhibit a mixture as a result of simultaneous local pollution and low  
250 concentration of mineral dust (Logothetis et al., 2020).

### 251 2.3 Copernicus Atmospheric Monitoring Service (CAMS)

252 We retrieved data from the CAMS radiation service (Schroedter-Homscheidt et al., 2022; Qu et al.,  
253 2017), from the solar radiation time-series product (CAMS, 2020). The CAMS solar radiation service  
254 provides historical estimates for global solar radiation, along with its components, from 2004 to  
255 present. These values are provided with a frequency as fine as 1-minute. In this study, we used the  
256 hourly time-series of GHI and DHI for all-sky conditions, setting the input coordinates to match the  
257 locations of the BSRN stations. The solar radiation time-series product (CAMS, 2020) performs  
258 interpolations integrated in its internal algorithm and provides time-series for the coordinates and  
259 the altitude of a single-site location. We compared the solar energy production derived from the use  
260 of CAMS data with that derived from the use of ground-based measurements from BSRN.

### 261 2.4 Radiative Transfer Model (RTM)

262 We performed Radiative Transfer (RT) simulations aiming to further assess the uncertainties in  
263 estimating the diffuse fraction arising from the effect of aerosols. The simulations were conducted  
264 using libRadtran (Emde et al., 2016; Mayer and Kylling, 2005), a widely used software package,  
265 allowing the computation of radiances, irradiances, and actinic fluxes. A sensitivity analysis was  
266 performed by comparing the diffuse irradiance calculated from libRadtran with the estimations of

267 BRL. This analysis examines the dependence of the aerosol-related discrepancy as function of Solar  
268 Zenith Angle (SZA) and latitude, considering the effect of parameters such as surface albedo and  
269 altitude.

270 To conduct aerosol parameterizations, we considered the default aerosol extinction profile (Shettle,  
271 1989) and set asymmetry factor (gg) to 0.7, while varying the Single Scattering Albedo (SSA) and the  
272 Ångström Exponent (AE), and defining  $AOD_{500}$  by adjusting the value of the parameter-b in  
273 Ångström's law (Ångström, 1929) as follows:

274 
$$\tau_\lambda = b \cdot \lambda^{-a} \rightarrow AOD_{500} = b \cdot (0.5 \mu m)^{-AE}(1)$$

275 The standard aerosol profiles (Anderson et al., 1986) were used for all sites. According to  
276 Fountoulakis et al. (2022), using a more accurate vertical distribution of aerosols in the troposphere  
277 would have a negligible effect in the GHI and DHI at the Earth's surface.

278 Table 3 illustrates the libRadtran settings used in this study.

279 **Table 3.** LibRadtran inputs

Parameter	Input
Atmospheric profile	Mid-latitude summer (April-September)/mid-latitude winter (October - March) (Anderson et al., 1986)
Extraterrestrial spectrum	(Kato et al. 1999)
Datetime	date and time input accompanied by project location coordinates
Altitude	0.1/2 km
Surface albedo	0.2 / 0.8
Number of streams	6
RT solver	sdisort (Buras et al., 2011)
AE	0 – 2 with step 1
SSA	0.7, 0.9, 1.0
gg	0.7
TOC (Total Ozone Column)	300 DU
Integrated Water Vapor	15 mm

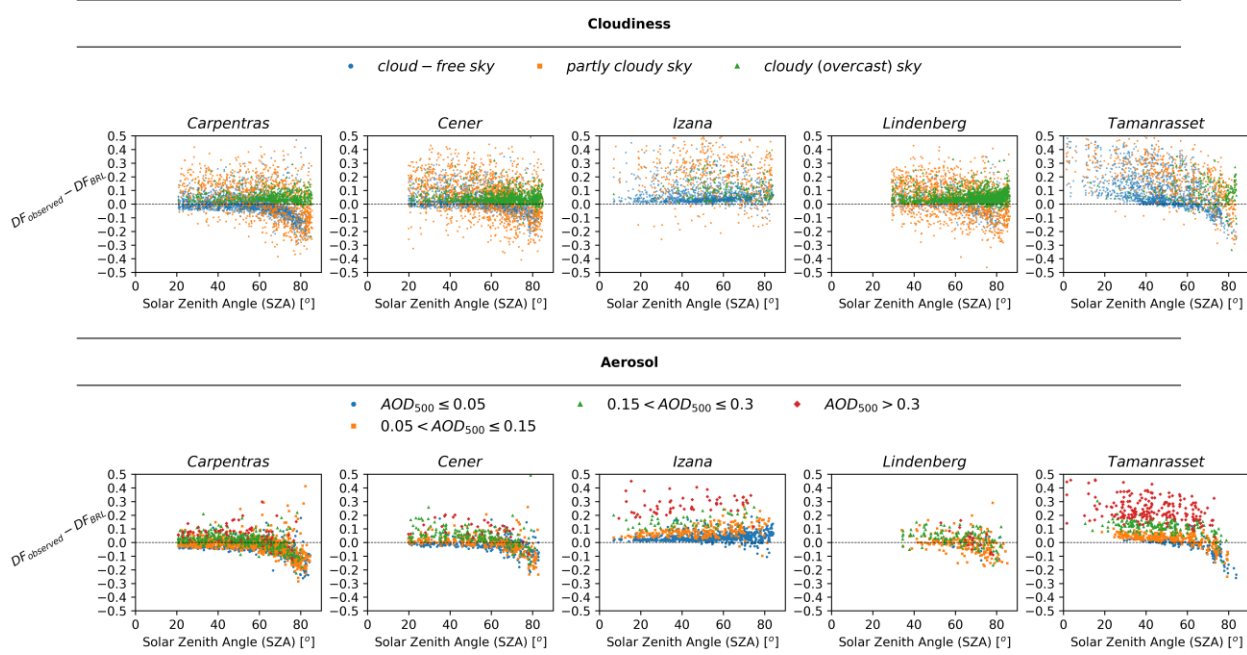
280

281 **3. Results**

282 3.1 Performance verification of the BRL diffuse fraction model

283 The performance of BRL was evaluated by comparing the actual diffuse fraction, obtained directly  
284 from resampled to hourly BSRN ground-based measurements, with that derived using BRL. As a first  
285 step, to isolate the influence of SZA from that associated with the atmospheric conditions, the  
286 difference in diffuse fraction (DF) between the observed and the one estimated using BRL as a  
287 function of SZA is presented in Figure 2. The atmospheric conditions are represented separately for  
288 both all-sky and cloud-free sky conditions and are grouped into clusters, as outlined in Section 2.2.  
289 The patterns reflecting the differences under the distinct sky conditions indicate an additional  
290 dependency on SZA, which becomes apparent approximately at SZA between 60° and 70°. In most  
291 cases, there is an almost constant displacement with respect to y=0 below 60°, as well as a change  
292 in behavior when SZA exceeds this value. Izaña presents a special case, as the station is located at  
293 a very high altitude. At such high altitudes the contribution of the diffuse component to the total  
294 irradiance is significantly smaller relative to lower altitude sites, which seems to be captured more  
295 accurately by BRL at high SZAs. We must also note that (i) at Izaña, the actual diffuse irradiance may  
296 experience an additional enhancement due to the contribution of adjacent lower-lying clouds – an  
297 effect that is not accounted for in the diffuse fraction model, and (ii) during dust events the site is  
298 usually inside – and not under – the dust layer, which results in more complex interactions between  
299 dust and solar radiation relative to lower altitude sites. Defining an exact limit (for the lower altitude  
300 sites), where the behavior is changing, is challenging; therefore, 60° was selected for practical  
301 energy-related applications, focusing on periods with meaningful energy contribution, and is  
302 supported by the sensitivity analysis (Section 3.2) under clear-sky conditions. Concerning the same  
303 grouped atmospheric conditions, Figure 3 illustrates the comparison between the observed and the  
304 estimated diffuse fraction for  $SZA \leq 60^\circ$ . This approach allows us to examine BRL performance after  
305 eliminating the influence of SZA, thereby providing a more comprehensive view of its reliability.

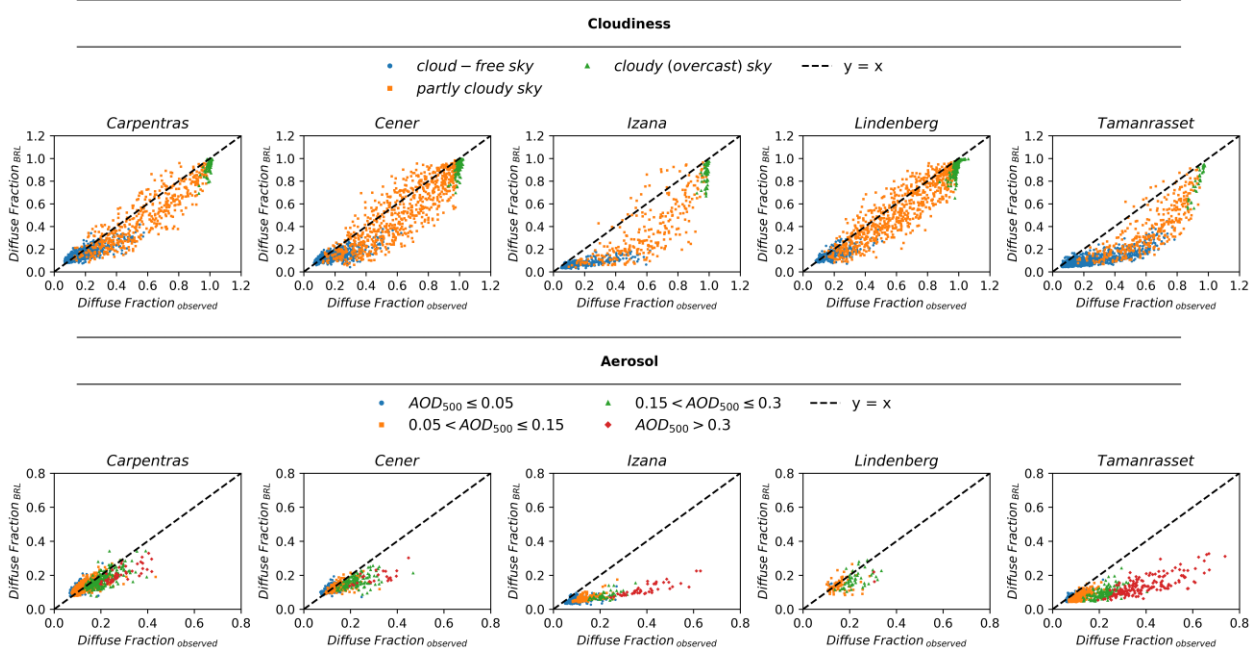
$$\text{Diffuse Fraction (DF) observed} - \text{Diffuse Fraction (DF)}_{\text{BRL}} = f(\text{sza})$$



306

307 **Figure 2.** Difference between the diffuse fraction estimated by the ground-based measurements  
 308 and by using the BRL model as a function of SZA under diverse atmospheric conditions: (top)  
 309 classification with respect to cloudiness and (bottom) classification with respect to aerosol optical  
 310 depth

$$\text{Diffuse Fraction (DF)}_{\text{BRL}} = f(\text{Diffuse Fraction (DF)}_{\text{observed}})$$



311

312       **Figure 3.** Comparison of the diffuse fraction estimated using BRL with that estimated by the  
313        ground-based measurements under diverse atmospheric conditions for  $SZA < 60^\circ$ : (top)  
314        classification with respect to cloudiness and (bottom) classification with respect to aerosol optical  
315        depth

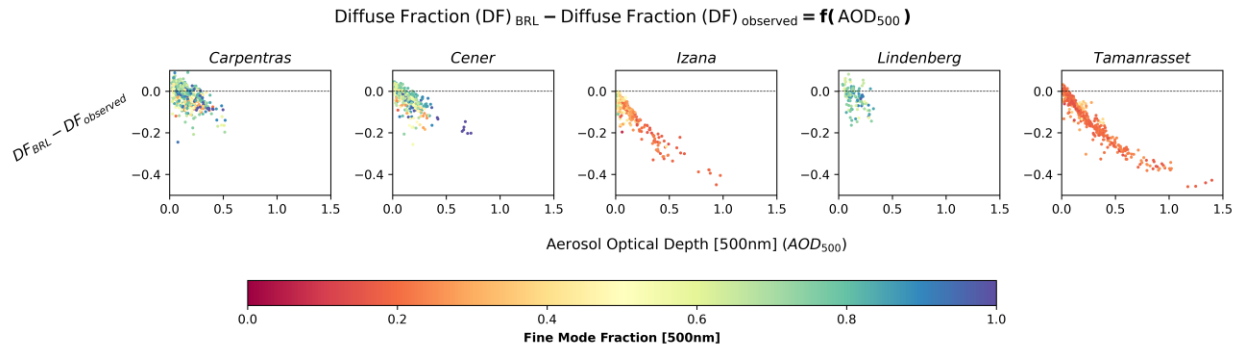
316

317       From Figure 3, a distinct dependency of BRL's reliability on the atmospheric conditions can be  
318       observed. Under all-sky conditions, the presence of clouds has a notable impact on the model's  
319       performance. Partly cloudy conditions result in greater dispersion of the values from the identity line  
320       respectively, likely due to the complexity of such sky scenes. Under overcast conditions, where the  
321       sky can be considered homogeneous and isotropic, the model in most cases performs slightly better.  
322       However, the limitations of the DNI-based classification methodology, related to the complexity of  
323       the cloud scenes, the spatiotemporal variability during the hourly periods, and the 3D variability of  
324       cloud properties, would require additional observational tools for a more detailed investigation. More  
325       specifically, the vast majority of overcast cases where the BRL diffuse fraction is below 0.8 while the  
326       observed is close to 1 correspond to periods involving rapid transitions between partly cloudy and  
327       overcast skies, occurring either during the hour itself or immediately before or after it. Furthermore,  
328       a limited number of cases identified during intense dust events at Tamanrasset and Izana, where the  
329       reduction of DNI was so pronounced that the applied DNI-based criterion classified these conditions  
330       as overcast. However, these cases are not further investigated, as the energy production levels during  
331       such periods are very low.

332       Under cloud-free skies, BRL tends to underestimate, and this bias becomes more pronounced as  
333       aerosol load increases. Aiming to highlight this dependency, Figure 4 shows the difference between  
334       the estimated and the observed diffuse fraction as function of  $AOD_{500}$ , emphasizing also the extent  
335       to which it is related to the aerosol type by providing  $FMF_{500}$ . A decrease for increasing  $AOD_{500}$  is  
336       evident across all cases. In Tamanrasset and Izaña, associated with the influence of Saharan dust,  
337       the coarse mode dominates, and a more distinct and well-defined curve is depicted compared to  
338       other sites.

339       It is important to clarify that for assessing the impact of aerosols we have assumed entirely cloud-  
340       free conditions. However, the criterion applied based on DNI does not fully guarantee the absence of  
341       small, scattered clouds within the sky dome. Such clouds could induce slight enhancements in DHI.

342 A more rigorous assessment of the impact associated exclusively with aerosols could be achieved  
 343 by integrating images from ground-based co-located all-sky cameras. On the other hand, the  
 344 presence of aerosols even under cloudy scenes, introduces an additional uncertainty which is  
 345 difficult to investigate accurately.



346

347 **Figure 4.** Difference between the estimated using BRL and the diffuse fraction estimated by the  
 348 ground-based measurements as function of  $AOD_{500}$  and  $FMF_{500}$

349

350 3.2 Sensitivity analysis of the BRL performance under cloud-free sky conditions from RT  
 351 simulations

352 The uncertainties in estimating diffuse fraction under cloud-free sky conditions, as discussed in  
 353 section 3.1, are further investigated. We performed RT simulations using libRadtran to calculate GHI  
 354 and DHI under various aerosol scenarios. The resulting GHI values were then used as input to BRL to  
 355 estimate the diffuse fraction, which was subsequently compared to the diffuse fraction derived  
 356 directly from the ratio of DHI to GHI computed by libRadtran.

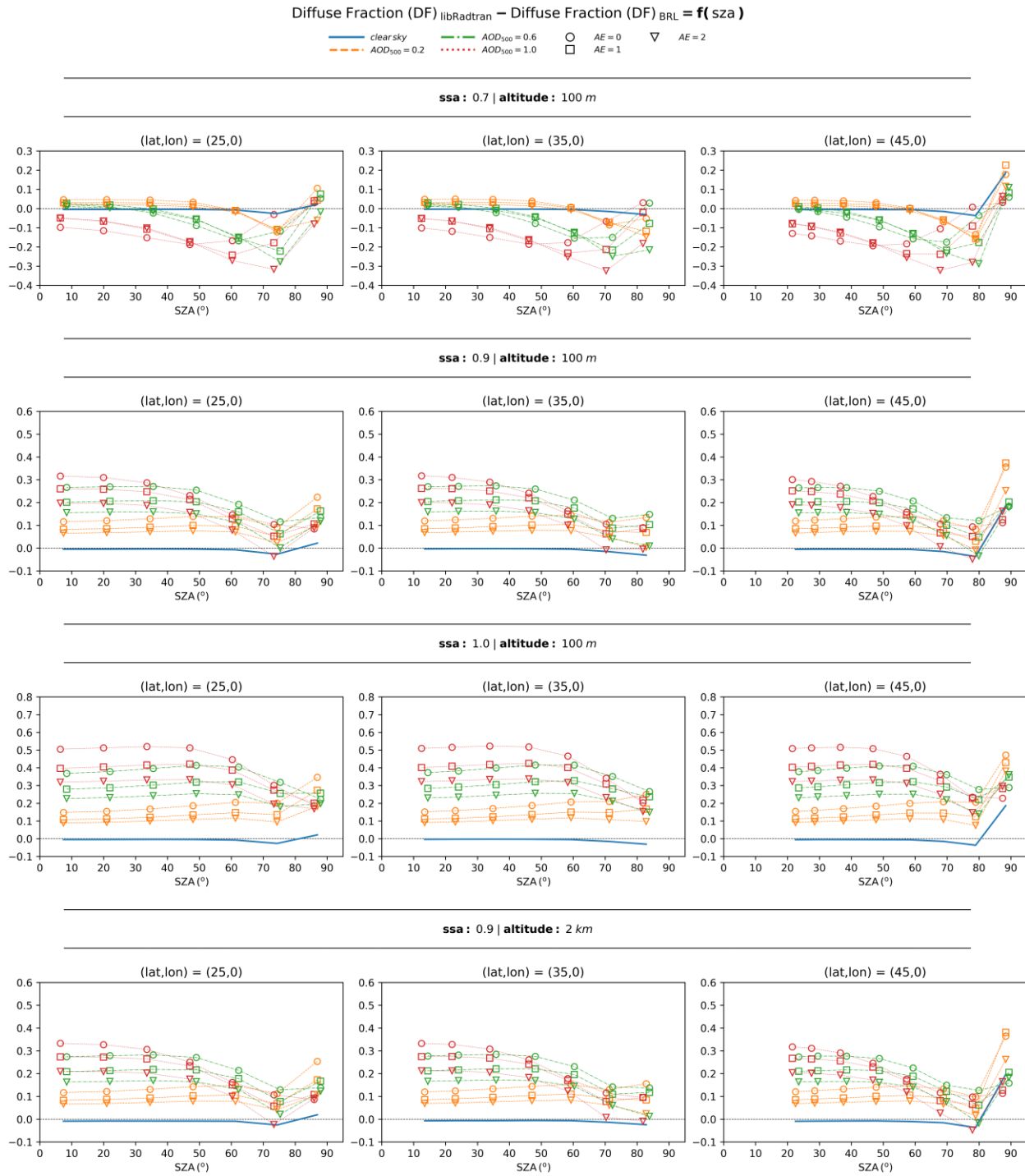
357 To ensure a comprehensive analysis, we considered three representative latitudes ( $25^\circ$ ,  $35^\circ$  and  $45^\circ$ ).  
 358 Since BRL requires an hourly time-series of GHI as input, the analysis was conducted for the summer  
 359 solstice. On this day, a sufficient number of hourly values are available, corresponding to a wide  
 360 range of SZA values, allowing for a robust assessment of the methodology. The sensitivity analysis  
 361 was performed for surface albedo values of 0.2 and 0.8 as well as for altitudes of 0.1 and 2 km. For  
 362 aerosol parameterization, we examined completely clear-sky conditions as a reference, alongside  
 363 scenarios with  $AOD_{500}$  values of 0.2, 0.6, and 1, while varying the SSA and AE. Specifically, the  
 364 scenarios included SSA values of 0.7, 0.9 and 1, combined with AE values of 0, 1 and 2. The results

365 of this sensitivity analysis for an albedo of 0.2 are provided in Figure 5, while the results for an albedo  
366 of 0.8 are included in the supplement (Figure S1).

367 The results confirm that BRL performs well under clear sky conditions and for SZA below 60°, while  
368 the incorporation of aerosols in the sky scene introduces larger uncertainties. In all scenarios, we  
369 observe that lower values of AE correspond to higher uncertainties. Moreover, when SSA is 0.9 or 1  
370 BRL gradually tends to underestimate the diffuse fraction as aerosol load increases. Instead, when  
371 SSA is 0.7, BRL exhibits a different behavior, shifting toward an overestimation of the diffuse fraction  
372 at high aerosol loads.

373 The findings of this sensitivity analysis are consistent with the evaluated BRL performance from  
374 ground-based measurements presented in section 3.1, especially at SZA smaller than 60° - 70°, and  
375 underscore the role of aerosol in the accuracy of diffuse fraction estimations. Differences between  
376 the results shown in Figures 2 and 5 at SZA between 60° - 80° can be due to a number of site-related  
377 reasons. For example, enhancement of the diffuse component due to scattering by underlying  
378 atmospheric layers and clouds in the case of Izaña may compensate the observed overestimation of  
379 the diffuse fraction by BRL. Concerning the impact related to AE and SSA, we confirm that the higher  
380 underestimations observed for Tamanrasset and Izaña are associated with the optical properties of  
381 desert dust aerosol particles. While AE and SSA alone are not sufficient to fully characterize the  
382 aerosol type, they serve as strong indicators, aligning with the classification framework of Dubovik et  
383 al. (2002). The same comparison for albedo 0.8 (Figure S1 in the supplement) reveals a significant  
384 broadening of the discrepancies. Moreover, we observe the presence of a systematic error, even  
385 under clear sky conditions.

386 The resulting differences were practically identical across the three selected latitudes, indicating  
387 that the BRL model is largely independent of latitude and can therefore be considered as a reliable  
388 solution over a wide range of latitudes. Furthermore, the effect of altitude was found to be small.  
389 Finally, the outcomes of this analysis highlight potential inconsistencies arising from aerosols with  
390 different optical properties. Although the updated parameters of the BRL's model (as implemented  
391 in the GSEE model) reported by Lauret et al. (2013) were derived using data from nine worldwide  
392 locations, encompassing a broad range of sky conditions that capture a fully representative set of  
393 optical properties remain challenging.



394

395 **Figure 5.** Difference between the diffuse fraction derived directly from the computations of DHI and  
396 GHI using libRadtran and the one estimated by applying BRL to the libRadtran-computed GHI

397

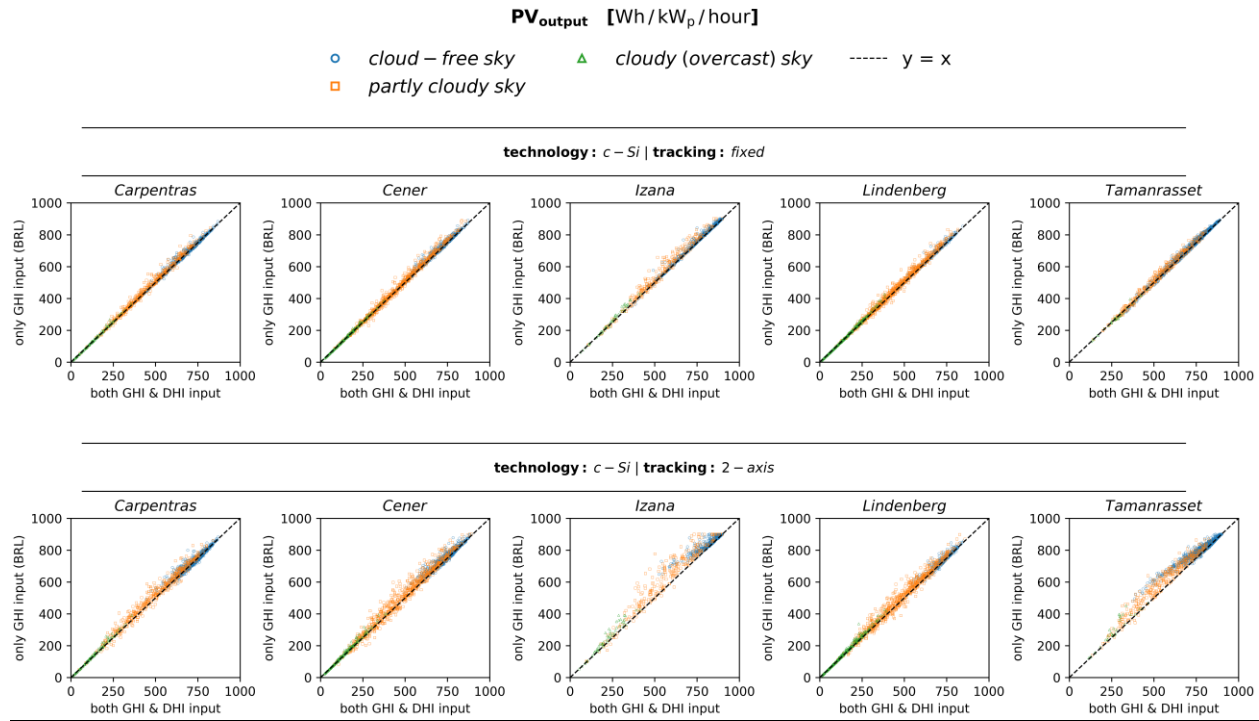
398

399 3.3 Analysis of the differences in energy production using hourly integrals within the modelling of PV  
400 plants

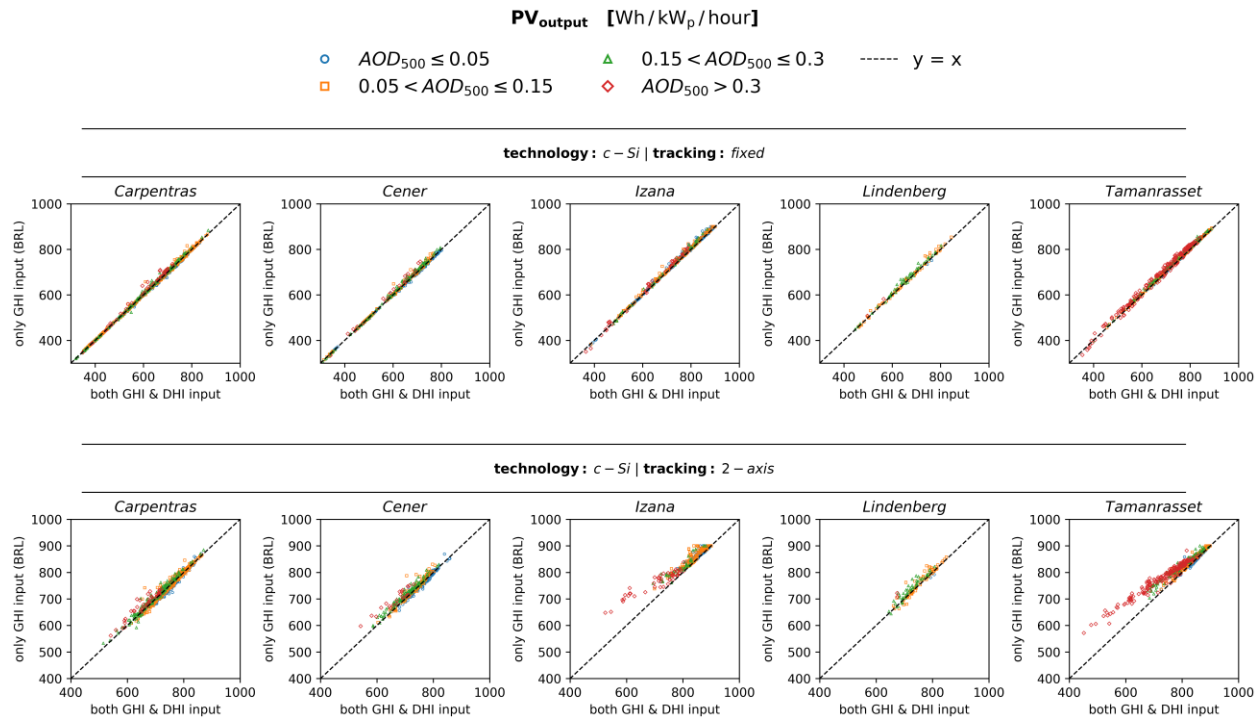
401 Uncertainties in estimating the diffuse fraction influence the calculation of the total irradiance  
402 received by an inclined panel's surface, thereby affecting the accuracy of the PV power simulations.  
403 In this section, we employ the main submodule of GSEE, used for modelling the electric output from  
404 a PV panel, aiming to assess the extent to which these uncertainties propagate to the estimation of  
405 the hourly power production. We analyze discrepancies arising from using only GHI from BSRN as  
406 input radiation data to the model, instead of both DHI and GHI. More specifically, we compare the  
407 total energy produced per hour per unit, expressed in watt-hours (Wh), per unit of nominal power  
408 (kWp). The energy production is evaluated for both fixed panels and 2-axis tracking systems.

409 The results of this comparison for c-Si based technology PV panels for different atmospheric  
410 conditions are presented in Figure 6, illustrating the impact of cloudiness, and in Figure 7,  
411 demonstrating the effect of aerosols. The corresponding results for CdTe technology are provided in  
412 the supplement (Figures S2 and S3 respectively). In the modelling of 2-axis solar tracking systems,  
413 where the panel is continuously adjusted to maintain a perpendicular orientation to incoming solar  
414 radiation, the system becomes more sensitive to uncertainties in the estimation of the diffuse  
415 fraction, leading to more significant differences in energy production. Specifically, the contribution  
416 of the direct irradiance is maximized in such systems, as the panel exploits the entirety of the  
417 available direct irradiance. On the other hand, in the simulation of static panels, the contributions of  
418 direct and diffuse components are more evenly distributed, making the impact of diffuse fraction  
419 uncertainties less pronounced in energy production.

420 Regarding the uncertainties related to the atmospheric conditions, from Figure 6 we confirm that the  
421 highest dispersion occurs in partly cloudy conditions, while from Figure 7, where we examine cloud-  
422 free conditions, we note that further improvement achieved as aerosol load decreases. Under totally  
423 overcast skies the energy production is extremely low, rendering errors practically negligible.  
424 Moreover, accuracy is influenced by aerosols, where a gradual decline in accuracy is detected as  
425 aerosol load increases. However, assessing the extent of aerosol loading impact is complex,  
426 depending on the interaction of solar radiation with particles of varying optical properties, as  
427 extensively analyzed in the previous sections. This effect becomes particularly evident in cases of  
428 high aerosol loading, where a noticeable offset is observed, while under certain conditions, the  
429 associated uncertainty is comparable to that found in partly cloudy conditions.



431 **Figure 6.** Comparison of the estimated hourly PV power generation between simulations performed  
 432 using GSEE with input data consisting of either only GHI or both GHI and DHI under varying  
 433 cloudiness conditions: (top) fixed panels (bottom) 2-axis tracking systems



435 **Figure 7.** Comparison of the estimated hourly PV power generation between simulations performed  
 436 using GSEE with input data consisting of either only GHI or both GHI and DHI under varying aerosol  
 437 conditions: (top) fixed panels (bottom) 2-axis tracking systems

438 The PV systems considered in this study have a nominal capacity of 1 kWp. The PV model applies a  
 439 default system loss factor of 10%. This effectively limits the maximum achievable power output to  
 440 approximately 90% of the nominal capacity (i.e., around 900 W/kWp). This effect becomes apparent  
 441 at the Izaña site due to its low latitude combined with its specific geographical and atmospheric  
 442 conditions, which lead to high irradiance levels. As a result, the simulated PV output in some cases  
 443 appears capped around 900 Wh/kWp per hour when only GHI is used.

444 Additionally, Tables 4 and 5 present the validation results for Carpentras and Tamanrasset, selected  
 445 as representative locations that encompass a wide variety of sky conditions. Validation results for  
 446 the remaining stations are available in the supplement (Tables S1-S3). All the evaluation metrics  
 447 correspond to simulations of PV panels with c-Si technology.

448 **Table 4.** Evaluation metrics for GSEE performance within hourly intervals in Carpentras, comparing  
 449 simulations with diffuse fraction from measurements and from the BRL model

STATION: Carpentras		fixed panels			2-axis tracking		
		RMSE (Wh/kWp/hour)	MAE (Wh/kWp/hour)	rMBE (%)	RMSE (Wh/kWp/hour)	MAE (Wh/kWp/hour)	rMBE (%)
All-Sky scenes		12.6	6.6	0.8	20.8	12.5	1.2
All-Sky scenes (cloudiness)	cloud-free	9.2	4.6	0.4	14.8	8.7	0.5
	partly cloudy	19.5	12.5	2.3	32.5	23.9	3.8
	cloudy (overcast)	5.8	3.0	2.0	10.5	6.1	4.6
Cloudless- Sky scenes (aerosol load)	low	4.7	3.4	-0.4	9.5	7.5	-0.8
	moderate	4.3	2.2	0.1	7.8	4.7	0.0
	high	6.4	4.0	0.6	11.0	7.8	0.9
	very high	14.9	10.2	1.6	22.7	17.2	2.6

450

451 **Table 5.** Evaluation metrics for GSEE performance within hourly intervals in Tamanrasset,  
 452 comparing simulations with diffuse fraction from measurements and from the BRL model.

STATION: Tamanrasset		fixed panels			2-axis tracking		
		RMSE (Wh/kWp/hour)	MAE (Wh/kWp/hour)	rMBE (%)	RMSE (Wh/kWp/hour)	MAE (Wh/kWp/hour)	rMBE (%)
All-Sky scenes		13.6	9.3	1.0	40.4	27.8	3.8

All-Sky scenes (cloudiness)	cloud-free	11.5	8.0	0.8	35.3	23.4	2.9
	partly cloudy	20.1	15.0	2.0	56.1	45.7	8.1
	cloudy (overcast)	8.4	5.2	-0.1	45.3	30.1	11.2
Cloudless-Sky scenes (aerosol load)	low	3.2	2.0	0.2	6.6	4.0	0.3
	moderate	5.4	4.6	0.6	13.0	10.5	1.2
	high	12.5	11.7	1.6	30.1	27.4	3.4
	very high	18.0	16.2	1.9	57.0	49.2	6.8

453

454 Based on the calculated statistical indices, the Root Mean Square Error (RMSE) values for fixed  
 455 panels range from 4.7 Wh/kWp/hour (clear sky) to 19.5 Wh/kWp/hour (partly cloudy) in Carpentras,  
 456 and from 3.2 to 20.1 Wh/kWp/hour in Tamanrasset. Under very high aerosol loading, RMSE reaches  
 457 14.9 and 18.0 Wh/kWp/hour, respectively. For 2-axis tracking systems, RMSE values vary  
 458 significantly, ranging from 9.5 to 32.5 Wh/kWp/hour in Carpentras and from 6.6 to 56.1 Wh/kWp/hour  
 459 in Tamanrasset, with peaks of 22.7 and 57.0 Wh/kWp/hour under very high aerosol loading  
 460 conditions. Similarly, the Mean Absolut Error (MAE) values are generally lower for fixed panels (3.4-  
 461 12.5 Wh/kWp//hour in Carpentras, 2.0-15.0 in Tamanrasset) and substantially higher for 2-axis  
 462 tracking (7.5-23.9 and 4.0-45.7 Wh/kWp/hour, respectively). Notably in Tamanrasset, MAE values  
 463 under very high aerosol loading exceed those observed under partly cloudy conditions, with values  
 464 increasing from 15.0 to 16.2 Wh/kWp/hour for fixed panels and from 45.7 to 49.2 Wh/kWp/hour for  
 465 2-axis tracking systems. Regarding the relative mean bias (rMBE), this remains mostly within  $\pm 4.6\%$   
 466 for fixed panels but can reach up to 11.2% for 2-axis tracking, particularly in aerosol-laden  
 467 conditions.

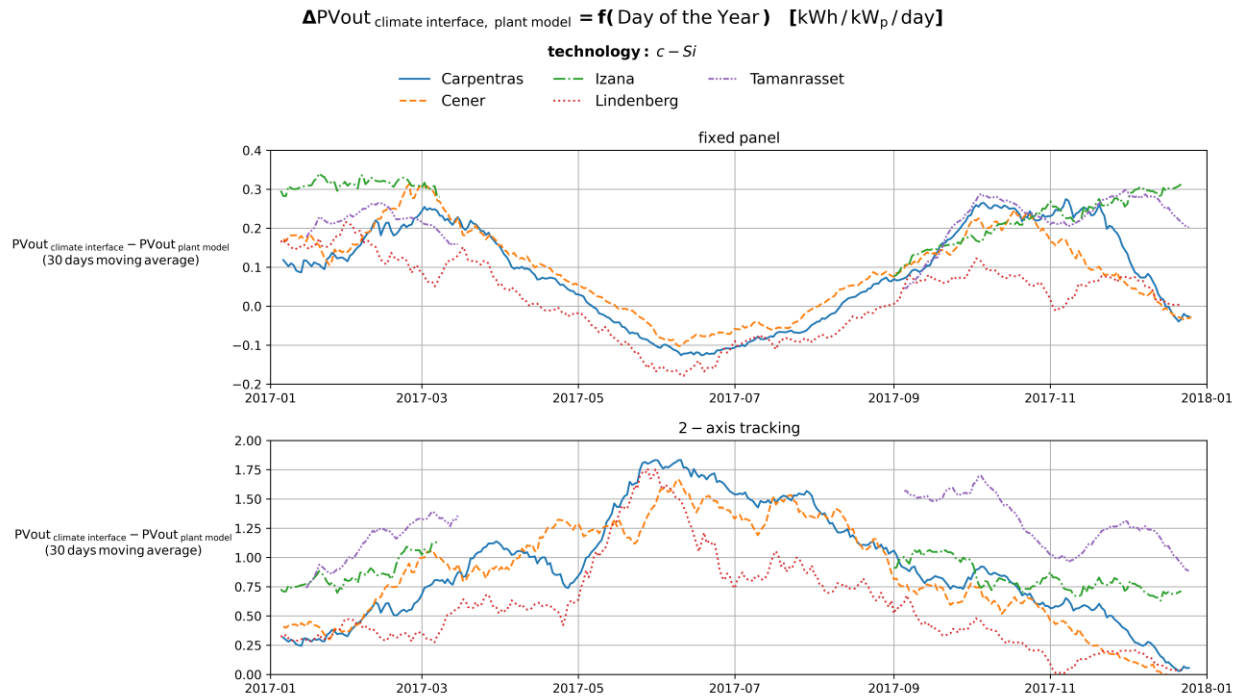
468

#### 469 3.4 Estimating total daily PV power output using the Climate Interface

470 Validation of the estimated daily energy production using the Climate Interface is achieved by  
 471 comparing the estimates with the results obtained from the direct summation of the hourly  
 472 simulations with input both GHI and DHI.

473 The Climate Interface generates the hourly profile of GHI for each day as a sinusoidal function. Then,  
 474 the BRL is applied to the hourly time-series, and the hourly power generation is computed. Finally,  
 475 these values are summed up to provide an estimate of the total daily output power. As shown in Fig.  
 476 8, which illustrates the differences between the Climate Interface estimates and the sums of the  
 477 hourly simulations, this approach introduces a variability throughout the year. Furthermore, Figure

478 S6 in the supplement presents the percentage differences between the two approaches, using the  
 479 latter as the reference.



480

481 **Figure 8.** Time-series of the differences between the daily PV output estimated using the climate  
 482 interface and the corresponding daily sums from hourly simulations.

483

484 The time-series represent the centered 30-day moving average. To ensure that the values are  
 485 representative of the reference period, we have applied all conditions requiring at least 20 days of  
 486 available data within each 30-days interval. In Tamanrasset and Izaña, especially during the summer  
 487 months, there are significant data gaps on several days, often occurring around solar noon.

488 More precisely, from Fig. 8, we observe that within the modelling of PV plants with fixed panels, there  
 489 is a tendency to overestimate in winter, with deviations of approximately 0.3 kWh/kWp/day, and to  
 490 slightly underestimate in summer, where deviations are around 0.1 kWh/kWp/day. In contrast, for 2-  
 491 axis solar tracking systems, the resulting deviations are significantly larger, with a general tendency  
 492 toward overestimation that peaks during summer, reaching approximately 1.75 kWh/kWp/day. The  
 493 percentage differences span from -10 to 20 % for fixed panels and from -5 to 35 % for 2-axis tracking  
 494 systems.

495 The variability in the percentage difference between the daily PV output estimated using the climate  
496 interface and the corresponding daily sums is mainly a function of the minimum SZA, while  
497 especially in the case of modeling for 2-axes tracking systems, the variation is also influenced by  
498 aerosol loading, with differences tending to increase as aerosol load rises (Figures S4 and S5 in the  
499 supplement).

500 Additional validation results are provided in the supplement (Tables S4-S8). Indicatively, for  
501 Carpentras and Tamanrasset, representative results are discussed below. For fixed panels, RMSE is  
502 minimized at 0.18 kWh/kWp/day under very-low aerosol conditions, compared to the overall 0.22  
503 kWh/kWp/day for Carpentras. In Tamanrasset, the lowest RMSE is observed at 0.15 kWh/kWp/day  
504 under very low aerosol conditions, while the overall reaches 0.24. In the case of 2-axis tracking, a  
505 significant increase is observed from low-aerosol to aerosol-laden conditions, ranging from 0.82 to  
506 1.28 kWh/kWp/day in Carpentras and from 0.66 to 1.37 in Tamanrasset. Similar widening trends are  
507 also evident in the MAE values across different aerosol loading conditions. The computed statistical  
508 indices confirm that the differences are minimized under sunny and nearly aerosol-free sky  
509 conditions. Comparing the performance on low-aerosol days to that on aerosol-laden, we conclude  
510 that, particularly in the case of modelling 2-axis tracking systems, errors increase significantly. In  
511 Tamanrasset, in particular, the errors are more than double.

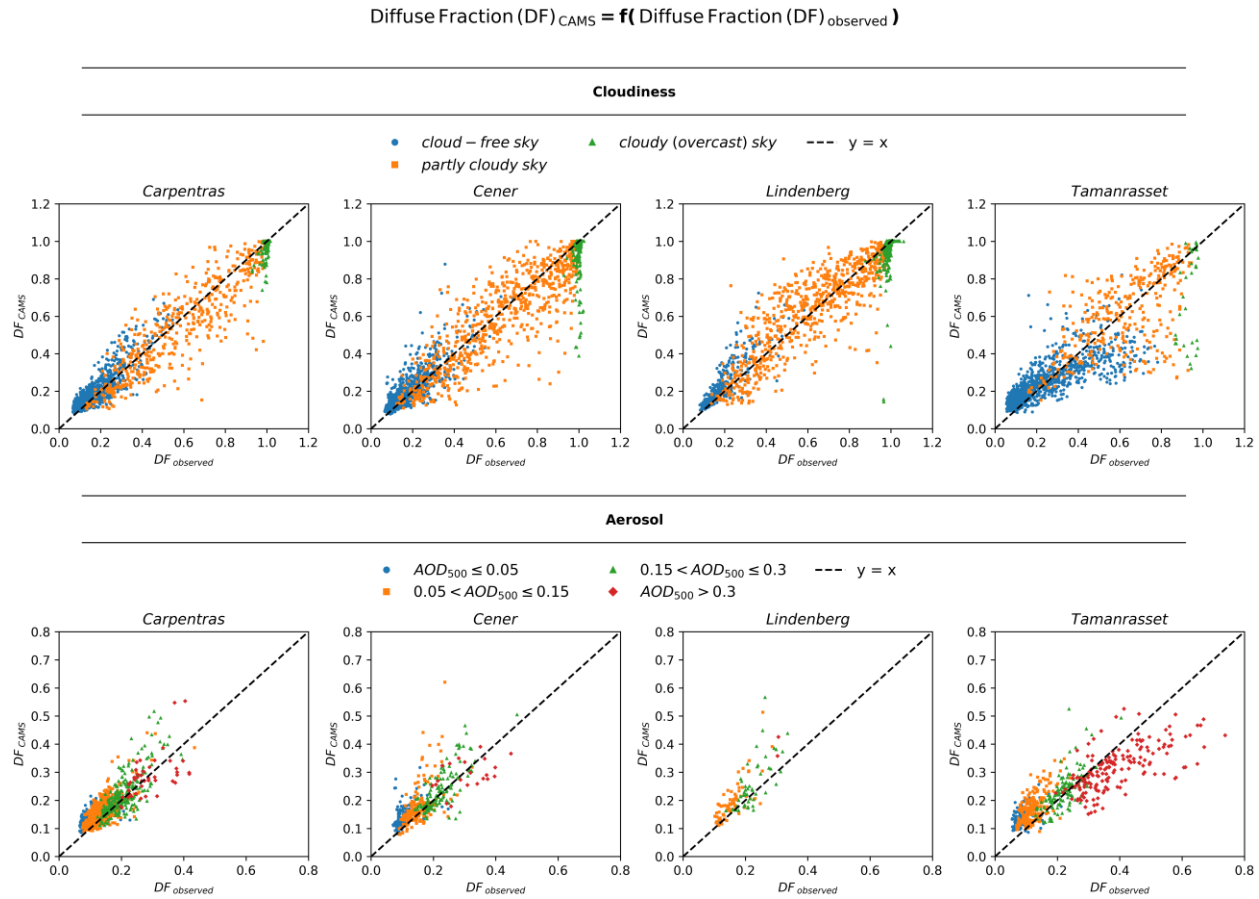
512 3.5 Evaluation of the reliability of using the CAMS solar radiation time-series product in modelling  
513 PV power potential

514 The aim of this section is to inspect the reliability of using the CAMS solar radiation time-series  
515 product in modelling the PV power potential adapted to a certain location. A review of the existing  
516 literature indicates a lack of studies directly examining the accuracy of using CAMS data for  
517 assessing PV power potential. This is addressed by comparing the output power obtained from using  
518 CAMS solar radiation data with that calculated using ground-based measurements. The analysis  
519 focuses on the capability of CAMS to provide accurate estimates of both GHI as well as its individual  
520 components.

521 In this section, we have excluded Izaña, because, due to its high altitude – as indicated through a  
522 personal communication with Yves-Marie Saint-Drenan (2025) – comparable results would require  
523 adjusting the measurements to the elevation of the stations, which is a complicated process and  
524 beyond the scope of this study.

525 The CAMS-based diffuse fraction, compared to the observed, is presented in Figure 9 under different  
 526 prevailing conditions. We observe that the calculation of the diffuse component is subject to  
 527 significant uncertainty. Cloudiness is the primary uncertainty source, particularly under partly cloudy  
 528 conditions. Additionally, notable discrepancies related to aerosols emerge only in cases of very high  
 529 aerosol loading.

530



531

532 **Figure 9.** Comparison of the CAMS-based diffuse fraction estimated using BRL with the actual one  
 533 under diverse atmospheric conditions

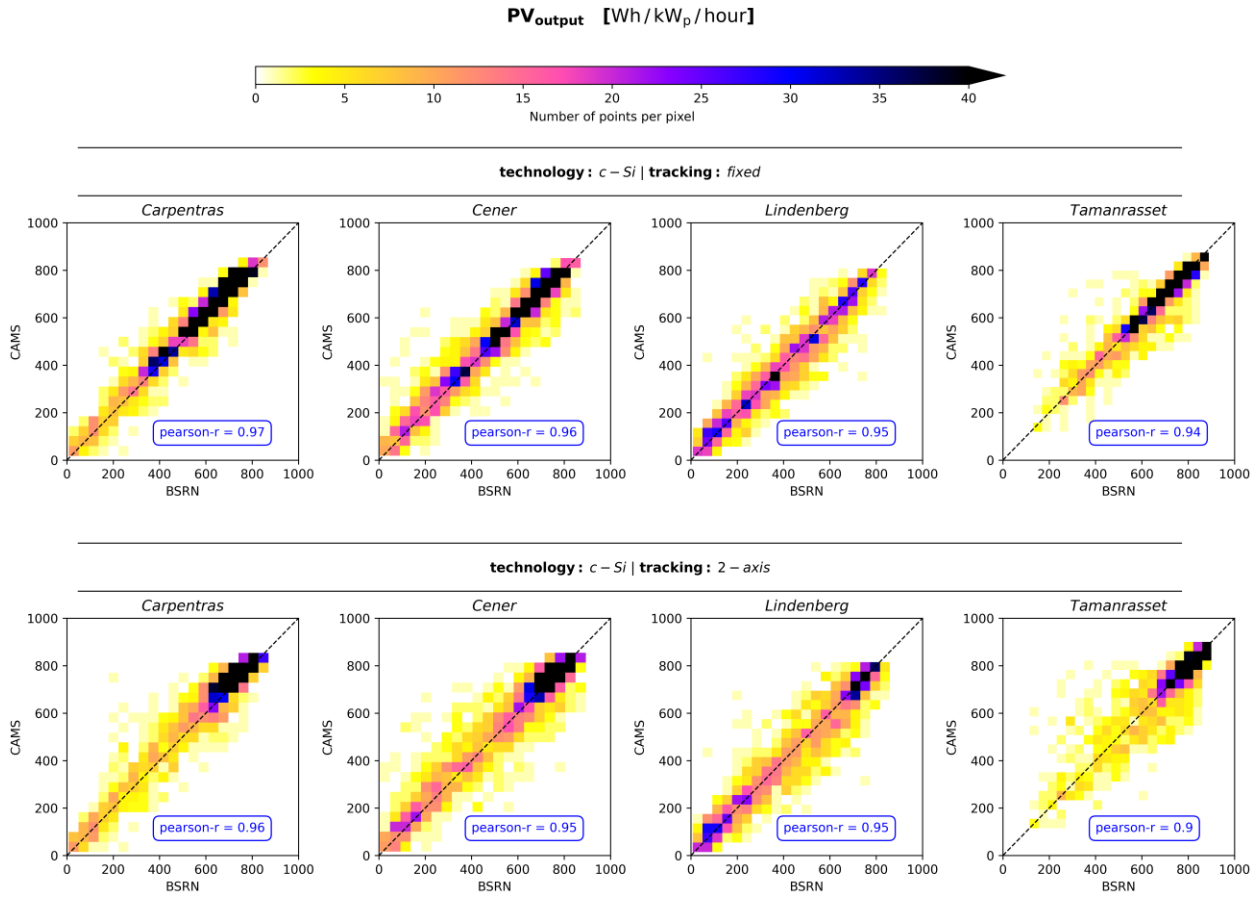
534

535 In Fig. 10 we provide density scatter plots comparing the CAMS-based PV output power with that  
 536 computed from the ground-based BSRN data, aiming to illustrate how the uncertainty in the diffuse  
 537 component estimates propagate to the calculation of power generation. Notably, there is a much  
 538 greater dispersion from the y=x line in the case of simulating PV plants with 2-axis tracking system,

539 compared to that within the modelling of fixed panels. This outcome is attributed to the increased  
540 sensitivity of the 2-axis tracking systems to the partitioning of global irradiance into its components.  
541 Nevertheless, correlation coefficients are in all cases better than 0.9.

542 Additional evaluation metrics are provided in the supplement (Tables S9-S12). Indicatively, we  
543 observe that under cloudless conditions, for fixed panels, RMSE ranges between 25.0 to 42.3  
544 Wh/kWp/hour in Carpentras and 16.6 and 31.0 Wh/kWp/hour in Tamanrasset, with variations linked  
545 to aerosol loading. Similarly, MAE ranges from 20.0 to 36.9 Wh/kWp/hour in Carpentras and 11.9 to  
546 22.9 Wh/kWp/hour in Tamanrasset. For 2-axis systems, RMSE and MAE follow similar trend, ranging  
547 from 28.8 to 49.9 Wh/kWp/hour and 22.3 to 44.1 Wh/kWp/hour, respectively, in Carpentras, and from  
548 20.8 to 48.0 Wh/kWp/hour and 15.3 to 35.5 Wh/kWp/hour, respectively, in Tamanrasset. Conversely,  
549 under cloudy conditions the errors are significantly increasing. In Carpentras, as well as in Cener,  
550 and Lindenberg (according to the corresponding tables in the supplement) the errors peak under  
551 partly cloudy conditions, with RMSE reaching up to 94.2 Wh/kWp/hour in Carpentras. However, in  
552 Tamanrasset, the highest errors occur under overcast conditions, where RMSE and MAE for 2-axis  
553 solar tracking systems reach 210.7 and 151.6 Wh/kWp/hour, respectively. This exception can be  
554 interpreted through Figure 15, which illustrates that in the rare overcast scenes in Tamanrasset,  
555 CAMS occasionally reports low diffuse fraction values instead of values close to 1, suggesting that  
556 CAMS did not accurately represent cloudiness in these cases.

557



558

559 **Figure 10.** Overview of the reliability of the CAMS-based PV power simulations

560

561 **4. Conclusions**

562 The optimal approach to include solar radiation information to PV power models such as GSEE is to  
 563 use actual in-situ measurements of global and diffuse solar irradiance. Since measurements of the  
 564 diffuse component are rarely available, it is common to use measurements of the GHI (if available)  
 565 and retrieve the diffuse component using a model such as BRL. In the absence of in-situ  
 566 measurements, other options include the use of datasets such as CAMS or even a radiative transfer  
 567 model, provided that atmospheric inputs such as clearness index, aerosol optical depth (AOD), and  
 568 other aerosol properties are available. This study evaluated these options and their implications for  
 569 PV modelling accuracy.

570 The results highlighted the importance of having precise information for the distribution of solar  
 571 irradiance among its components in PV power modelling. The implementation of the BRL diffuse

572 fraction within GSEE serves as a practical, and under certain conditions, reliable solution to the  
573 absence of detailed information for each component separately. Moreover, the integrated Climate  
574 Data Interface submodule offers valuable prospects for investigating fluctuations in the solar PV  
575 power generation across various timescales. In this context, the use of BRL has a key contribution  
576 alongside the other computational procedures in processing climate datasets. Previous studies on  
577 PV power modelling approaches have not examined their reliability under diverse atmospheric  
578 conditions, including the effects associated with cloudiness, aerosol loading, as well as aerosol  
579 optical properties.

580 The evaluation of the BRL's performance revealed a dependency of its reliability on the prevailing sky  
581 conditions. BRL has excellent accuracy under totally clear sky scenes and still performs well for  
582 cloudless scenes with moderate aerosol loading. In general, its accuracy is inversely proportional to  
583 the complexity of the cloud scene. However, the model systematically underestimates the diffuse  
584 fraction under high-loading conditions, such as during dust events. The discrepancies arising from  
585 diffuse fraction estimation propagate to PV power generation and become particularly pronounced  
586 in the modelling of 2-axis tracking systems. Indicatively, MAE under cloud-free scenes with moderate  
587 aerosol loading, ranges between 2.2 to 6.6 Wh/kWp/hour for fixed panels and 4.7 to 15.0  
588 Wh/kWp/hour for 2-axis tracking systems. Under partly cloudy conditions, where the cloud scene is  
589 more complex, the MAE increases substantially, ranging from 12.4 to 25.8 Wh/kWp/hour for fixed  
590 panels and from 23.5 to 55.1 Wh/kWp/hour for 2-axis tracking systems. Moreover, during intense dust  
591 events, MAE can reach up to 49.2 Wh/kWp/hour in Tamanrasset, which is comparable to that  
592 computed under partly cloudy conditions. Overall, the rMBE remains within the  $\pm 5\%$ , with the  
593 exception of a limited cases under overcast conditions. The same analysis applied to CdTe panels  
594 yielded similar results, with minor differences.

595 Aiming to provide an indicative assessment of the financial impacts of the effect of desert dust  
596 aerosols, we assume that the statistical indices calculated for Tamanrasset are representative of a  
597 large-scale solar farm located in the Sahara region, with 500 MW installed PV capacity and systems  
598 equipped with 2-axis solar tracking system. For this hypothetical solar farm, according to the value  
599 of the Mean Absolute Error (MAE) on Table 4 for very high aerosol loading, we estimate that the  
600 produced energy is  $0.0492 [\text{kWh}/\text{kWp}/\text{hour}] \times 500 \times 10^3 [\text{kWp}] = 24600 [\text{kWh}/\text{hour}]$   
601 *supposing 12 sunlight hours per day*  $\underline{\underline{\rightarrow}} \sim 295200 [\text{kWh}/\text{day}]$  less than the expected from the PV power  
602 simulations. According to the global average auction prices for selling produced energy back to the

603 grid in 2021 (IRENA, 2026), the overestimations are equivalent to a financial loss of  
604  $0.039 \text{ [USD/kWh]} \times 295200 \text{ [kWh/day]} \approx 11,500 \text{ USD/day}$ . Therefore, site assessments that do  
605 not correctly account for the distribution of surface solar irradiance in the sky under desert dust  
606 aerosol conditions may overestimate financial performance and the annual financial deficit could be  
607 accumulated to hundreds of thousands of US dollars per year.

608 Comparing the range of computed errors, we observe that the errors arising from employing CAMS  
609 rather than using ground-based measurements, even when the diffuse fraction is not provided, are  
610 higher across the overwhelming majority of the considered sky conditions. More specifically,  
611 regarding the overall performance, MAE when using CAMS ranges between 33.7 and 46.1  
612 Wh/kWp/hour, while with ground-based GHI measurements, MAE remains below 10 Wh/kWp/hour  
613 within the modelling of systems with fixed panels and can reach up to 27.8 Wh/kWp/hour within the  
614 modelling of 2-axis tracking systems. This outcome highlights the value of ground-based  
615 measurements.

616 To sum up, achieving the highest quality PV power simulations necessitates high-quality, concurrent  
617 measurements of solar irradiance components. In absence of this, the submodules included in the  
618 GSEE package enable reliable simulations under the vast majority of prevailing sky conditions. CAMS  
619 serves as a valuable data source for PV power modelling, but it cannot fully replace the precision and  
620 reliability of using ground-based measurements. The integration of aerosol correction within the BRL  
621 model opens new possibilities for further improvements in the modelling of solar energy systems. A  
622 more comprehensive assessment would require measured PV output data; however, acquiring  
623 simultaneous direct and diffuse irradiance measurements at the same location as the solar farms  
624 remains challenging.

625

## 626 **Data availability**

627 The BSRN data are freely available on the BSRN web-page (<https://bsrn.awi.de/>). The AERONET  
628 version 3 products are freely available from the AERONET website (<https://aeronet.gsfc.nasa.gov/>).  
629 The CAMS radiation time-series are available from the Atmosphere Data Store  
630 (<https://ads.atmosphere.copernicus.eu>). The rest of the data used in this paper are available upon  
631 request from the authors.

## 632 **Author Contributions**

633 Conceptualization: NP and IF; Data curation: NP and KP; Formal analysis: NP; Funding acquisition:  
634 CZ; Investigation: NP; Methodology: NP, IF, SK, AK and AG; Project administration: CZ; Resources: SP,  
635 KP and LD; Software: NP; Supervision: IF; Validation: NP, IF and SP; Visualization: NP; Writing –  
636 original draft: NP; Writing – review & editing: all authors

637 **Funding**

638 This work has been supported by the action titled “Support for upgrading the operation of the  
639 National Network for Climate Change (CLIMPACT II)”, funded by the Public Investment Program of  
640 Greece, General Secretary of Research and Technology/Ministry of Development and Investments.  
641 Part of this work was also supported by the COST Action Harmonia (CA21119) supported by COST  
642 (European Cooperation in Science and Technology). This work was partially funded by the  
643 Copernicus Climate Change Service under contracts C3S2 \_461-1\_GR (Seasonal to decadal  
644 predictions for national renewable energy management).

645 **Acknowledgments**

646 We thank the teams of the AERONET for ground measurements and maintenance, and CAMS for the  
647 data production and distribution. We would like to thank the five site instrument operators and  
648 technical staff of the BSRN network stations who made the ground-based measurements feasible.  
649 A. Gkikas, J. Kapsomenakis, and C.S. Zerefos also acknowledge “CAMS2\_82 Project: Evaluation and  
650 Quality Control (EQC) of global products.”

651 **References**

652 Anderson, G. P., Clough, S. A., Kneizys, F. X., Chetwynd, J. H., and Shettle, E. P.: AFGL atmospheric  
653 constituent profiles (0.120 km), Air Force Geophysics Lab Hanscom AFB MA, 1986.  
654 Anderson, K. S., Hansen, C. W., Holmgren, W. F., Jensen, A. R., Mikofski, M. A., and Driesse, A.: pvlib  
655 python: 2023 project update, *J. Open Source Softw.*, 8, 5994, <https://doi.org/10.21105/joss.05994>,  
656 2023.  
657 Ångström, A.: On the Atmospheric Transmission of Sun Radiation and on Dust in the Air,  
658 *Geografiska Annaler*, 11, 156–166, <https://doi.org/10.1080/20014422.1929.11880498>, 1929.  
659 Barreto, A., García, R. D., Guirado-Fuentes, C., Cuevas, E., Almansa, A. F., Milford, C., Toledano, C.,  
660 Expósito, F. J., Díaz, J. P., and León-Luis, S. F.: Aerosol characterisation in the subtropical eastern

661 North Atlantic region using long-term AERONET measurements, *Atmos. Chem. Phys.*, 22, 11105–  
662 11124, <https://doi.org/10.5194/acp-22-11105-2022>, 2022.

663 Blaga, R., Mares, O., Paulescu, E., Boata, R., Sabadus, A., Hategan, S.-M., Calinouiu, D., Stefu, N.,  
664 and Paulescu, M.: Diffuse fraction as a tool for exploring the sensitivity of parametric clear-sky  
665 models to changing aerosol conditions, *Solar Energy*, 277, 112731,  
666 <https://doi.org/10.1016/j.solener.2024.112731>, 2024.

667 Blanc, P., Remund, J., and Vallance, L.: Short-term solar power forecasting based on satellite  
668 images, in: *Renewable Energy Forecasting*, Elsevier, 179–198, <https://doi.org/10.1016/B978-0-08-100504-0.00006-8>, 2017.

670 Boland, J., Scott, L., and Luther, M.: Modelling the diffuse fraction of global solar radiation on a  
671 horizontal surface, *Environmetrics*, 12, 103–116, [https://doi.org/10.1002/1099-095X\(200103\)12:2<103::AID-ENV447>3.0.CO;2-2](https://doi.org/10.1002/1099-095X(200103)12:2<103::AID-ENV447>3.0.CO;2-2), 2001.

673 Buras, R., Dowling, T., and Emde, C.: New secondary-scattering correction in DISORT with  
674 increased efficiency for forward scattering, *J. Quant. Spectrosc. Radiat. Transf.*, 112, 2028–2034,  
675 <https://doi.org/10.1016/j.jqsrt.2011.03.019>, 2011.

676 Cañadillas-Ramallo, D., Moutaoikil, A., Shephard, L. E., and Guerrero-Lemus, R.: The influence of  
677 extreme dust events in the current and future 100% renewable power scenarios in Tenerife, *Renew.  
678 Energy*, 184, 948–959, <https://doi.org/10.1016/j.renene.2021.12.013>, 2022.

679 Copernicus Atmospheric Monitoring Service (CAMS): CAMS solar radiation time-series, Copernicus  
680 Atmosphere Monitoring Service (CAMS) Atmosphere Data Store [data set], <https://doi.org/10.24381/5cab0912>, 2020.

682 Cuevas, E., Romero-Campos, P. M., Kouremeti, N., Kazadzis, S., Räisänen, P., García, R. D., Barreto,  
683 A., Guirado-Fuentes, C., Ramos, R., Toledano, C., Almansa, F., and Gröbner, J.: Aerosol optical  
684 depth comparison between GAW-PFR and AERONET-Cimel radiometers from long-term (2005–  
685 2015) 1 min synchronous measurements, *Atmos. Meas. Tech.*, 12, 4309–4337,  
686 <https://doi.org/10.5194/amt-12-4309-2019>, 2019.

687 Driemel, A., Augustine, J., Behrens, K., Colle, S., Cox, C., Cuevas-Agulló, E., Denn, F. M., Duprat, T.,  
688 Fukuda, M., Grobe, H., Haeffelin, M., Hodges, G., Hyett, N., Ijima, O., Kallis, A., Knap, W., Kustov, V.,  
689 Long, C. N., Longenecker, D., Lupi, A., Maturilli, M., Mimouni, M., Ntsangwane, L., Ogihara, H.,

690 Olano, X., Olefs, M., Omori, M., Passamani, L., Pereira, E. B., Schmithüsen, H., Schumacher, S.,  
691 Sieger, R., Tamlyn, J., Vogt, R., Vuilleumier, L., Xia, X., Ohmura, A., and König-Langlo, G.: Baseline  
692 Surface Radiation Network (BSRN): structure and data description (1992–2017), *Earth Syst. Sci.*  
693 *Data*, 10, 1491–1501, <https://doi.org/10.5194/essd-10-1491-2018>, 2018.

694 Dubey, S., Sarvaiya, J. N., and Seshadri, B.: Temperature Dependent Photovoltaic (PV) Efficiency  
695 and Its Effect on PV Production in the World – A Review, *Energy Procedia*, 33, 311–321,  
696 <https://doi.org/10.1016/j.egypro.2013.05.072>, 2013.

697 Dubovik, O. and King, M. D.: A flexible inversion algorithm for retrieval of aerosol optical properties  
698 from Sun and sky radiance measurements, *Journal of Geophysical Research: Atmospheres*, 105,  
699 20673–20696, <https://doi.org/10.1029/2000JD900282>, 2000.

700 Dubovik, O., Holben, B., Eck, T. F., Smirnov, A., Kaufman, Y. J., King, M. D., Tanré, D., and Slutsker, I.:  
701 Variability of Absorption and Optical Properties of Key Aerosol Types Observed in Worldwide  
702 Locations, *J. Atmos. Sci.*, 59, 590–608, [https://doi.org/10.1175/1520-0469\(2002\)059<0590:VOAAOP>2.0.CO;2](https://doi.org/10.1175/1520-0469(2002)059<0590:VOAAOP>2.0.CO;2), 2002.

704 Edenhofer, O., Pichs-Madruga, R., Sokona, Y., Seyboth, K., Matschoss, P., Kadner, S., Zwickel, T.,  
705 Eickemeier, P., Hansen, G., and Schlömer, S.: *IPCC special report on renewable energy sources and*  
706 *climate change mitigation*, Prepared By Working Group III of the Intergovernmental Panel on  
707 *Climate Change*, Cambridge University Press, Cambridge, UK, ISBN 978-1-107- 02340-6, 2011.

708 Emde, C., Buras-Schnell, R., Kylling, A., Mayer, B., Gasteiger, J., Hamann, U., Kylling, J., Richter, B.,  
709 Pause, C., Dowling, T., and Bugliaro, L.: The libRadtran software package for radiative transfer  
710 calculations (version 2.0.1), *Geosci. Model Dev.*, 9, 1647–1672, <https://doi.org/10.5194/gmd-9-1647-2016>, 2016.

712 Faid, A., Smara, Y., Caselles, V., and Khireddine, A.: Evaluation of the Saharan Aerosol Impact on  
713 Solar Radiation over the Tamanrasset Area, Algeria, *IJARET*, 3, 24–32, 2012.

714 Fountoulakis, I., Kosmopoulos, P., Papachristopoulou, K., Raptis, I.-P., Mamouri, R.-E., Nisantzi, A.,  
715 Gkikas, A., Witthuhn, J., Bley, S., Moustaka, A., Buehl, J., Seifert, P., Hadjimitsis, D. G., Kontoes, C.,  
716 and Kazadzis, S.: Effects of Aerosols and Clouds on the Levels of Surface Solar Radiation and Solar  
717 Energy in Cyprus, *Remote Sens. (Basel)*, 13, 2319, <https://doi.org/10.3390/rs13122319>, 2021.

718 Fountoulakis, I., Papachristopoulou, K., Proestakis, E., Amiridis, V., Kontoes, C., and Kazadzis, S.:  
719 Effect of Aerosol Vertical Distribution on the Modeling of Solar Radiation, *Remote Sens.* (Basel).,  
720 14, 1143, <https://doi.org/10.3390/rs14051143>, 2022.

721 Giles, D. M., Sinyuk, A., Sorokin, M. G., Schafer, J. S., Smirnov, A., Slutsker, I., Eck, T. F., Holben, B.  
722 N., Lewis, J. R., Campbell, J. R., Welton, E. J., Korkin, S. V., and Lyapustin, A. I.: Advancements in the  
723 Aerosol Robotic Network (AERONET) Version 3 database – automated near-real-time quality control  
724 algorithm with improved cloud screening for Sun photometer aerosol optical depth (AOD)  
725 measurements, *Atmos. Meas. Tech.*, 12, 169–209, <https://doi.org/10.5194/amt-12-169-2019>, 2019.

726 GSEE: Climate Data Interface documentation: <https://gsee.readthedocs.io/en/latest/climatedata->  
727 interface/, last access: 6 February 2026.

728 Holben, B. N., Eck, T. F., Slutsker, I., Tanré, D., Buis, J. P., Setzer, A., Vermote, E., Reagan, J. A.,  
729 Kaufman, Y. J., Nakajima, T., Lavenu, F., Jankowiak, I., and Smirnov, A.: AERONET—A Federated  
730 Instrument Network and Data Archive for Aerosol Characterization, *Remote Sens. Environ.*, 66, 1–  
731 16, [https://doi.org/10.1016/S0034-4257\(98\)00031-5](https://doi.org/10.1016/S0034-4257(98)00031-5), 1998.

732 Hou, X., Wild, M., Folini, D., Kazadzis, S., and Wohland, J.: Climate change impacts on solar power  
733 generation and its spatial variability in Europe based on CMIP6, *Earth System Dynamics*, 12, 1099–  
734 1113, <https://doi.org/10.5194/esd-12-1099-2021>, 2021.

735 Huld, T., Gottschalg, R., Beyer, H. G., and Topič, M.: Mapping the performance of PV modules,  
736 effects of module type and data averaging, *Solar Energy*, 84, 324–338,  
737 <https://doi.org/10.1016/j.solener.2009.12.002>, 2010.

738 IPCC: Summary for Policymakers, edited by: Pörtner, H.-O., Roberts, D. C., Poloczanska, E. S.,  
739 Mintenbeck, K., Tignor, M., Alegria, A., Craig, M., Langsdorf, S., Löschke, S., Möller, V., and Okem, A.,  
740 in: Climate Change 2022: Impacts, Adaptation and Vulnerability, Contribution of Working Group II  
741 to the Sixth Assessment Report of the Intergovernmental Panel on Climate Change, edited by:  
742 Pörtner, H.-O., Roberts, D. C., Tignor, M., Poloczanska, E. S., Mintenbeck, K., Alegria, A., Craig, M.,  
743 Langsdorf, S., Löschke, S., Möller, V., Okem, A., and Rama, B., Cambridge University Press,  
744 Cambridge, UK and New York, NY, USA, 3–33, <https://doi.org/10.1017/9781009325844.001>, 2022.

745 International Renewable Energy Agency (IRENA): Global LCOE and Auction Values:  
746 <https://www.irena.org/Data/View-data-by-topic/Costs/Global-LCOE-and-Auction-values>, last  
747 access: 6 February 2026.

748 Jacovides, C. P., Tymvios, F. S., Assimakopoulos, V. D., and Kaltsounides, N. A.: Comparative study  
749 of various correlations in estimating hourly diffuse fraction of global solar radiation, *Renew. Energy*,  
750 31, 2492–2504, <https://doi.org/10.1016/j.renene.2005.11.009>, 2006.

751 Kakran, S., Rathore, J. S., Sidhu, A., and Kumar, A.: Solar energy advances and CO<sub>2</sub> emissions: A  
752 comparative review of leading nations' path to sustainable future, *J. Clean. Prod.*, 475, 143598,  
753 <https://doi.org/10.1016/j.jclepro.2024.143598>, 2024.

754 Kato, S., Ackerman, T. P., Mather, J. H., and Clothiaux, E. E.: The k-distribution method and  
755 correlated-k approximation for a shortwave radiative transfer model, *J. Quant. Spectrosc. Radiat.*  
756 *Transf.*, 62, 109–121, [https://doi.org/10.1016/S0022-4073\(98\)00075-2](https://doi.org/10.1016/S0022-4073(98)00075-2), 1999.

757 Kazantzidis, A., Tzoumanikas, P., Blanc, P., Massip, P., Wilbert, S., and Ramirez-Santigosa, L.: Short-  
758 term forecasting based on all-sky cameras, in: *Renewable Energy Forecasting*, Elsevier, 153–178,  
759 <https://doi.org/10.1016/B978-0-08-100504-0.00005-6>, 2017.

760 Kosmopoulos, P., Kazadzis, S., El-Askary, H., Taylor, M., Gkikas, A., Proestakis, E., Kontoes, C., and  
761 El-Khayat, M.: Earth-Observation-Based Estimation and Forecasting of Particulate Matter Impact  
762 on Solar Energy in Egypt, *Remote Sens. (Basel)*, 10, 1870, <https://doi.org/10.3390/rs10121870>,  
763 2018.

764 Kouklaki, D., Kazadzis, S., Raptis, I.-P., Papachristopoulou, K., Fountoulakis, I., and Eleftheratos, K.:  
765 Photovoltaic Spectral Responsivity and Efficiency under Different Aerosol Conditions, *Energies*  
766 (Basel), 16, 6644, <https://doi.org/10.3390/en16186644>, 2023.

767 Lauret, P., Boland, J., and Ridley, B.: Bayesian statistical analysis applied to solar radiation  
768 modelling, *Renew. Energy*, 49, 124–127, <https://doi.org/10.1016/j.renene.2012.01.049>, 2013.

769 Liu, B. Y. H. and Jordan, R. C.: The interrelationship and characteristic distribution of direct, diffuse  
770 and total solar radiation, *Solar Energy*, 4, 1–19, [https://doi.org/10.1016/0038-092X\(60\)90062-1](https://doi.org/10.1016/0038-092X(60)90062-1),  
771 1960.

772 Logothetis, S.-A., Salamalikis, V., and Kazantidis, A.: Aerosol classification in Europe, Middle East,  
773 North Africa and Arabian Peninsula based on AERONET Version 3, *Atmos. Res.*, 239, 104893,  
774 <https://doi.org/10.1016/j.atmosres.2020.104893>, 2020.

775 Long, C. N. and Dutton, E. G.: BSRN Global Network recommended QC tests, V2.x,  
776 [https://epic.awi.de/id/eprint/30083/1/BSRN\\_recommended\\_QC\\_tests\\_V2.pdf](https://epic.awi.de/id/eprint/30083/1/BSRN_recommended_QC_tests_V2.pdf) (last access: 6  
777 February 2026), 2010.

778 Mayer, B. and Kylling, A.: Technical note: The libRadtran software package for radiative transfer  
779 calculations - description and examples of use, *Atmos. Chem. Phys.*, 5, 1855–1877,  
780 <https://doi.org/10.5194/acp-5-1855-2005>, 2005.

781 McMahan, A. C., Grover, C. N., and Vignola, F. E.: Evaluation of Resource Risk in Solar-Project  
782 Financing, in: *Solar Energy Forecasting and Resource Assessment*, Elsevier, 81–95,  
783 <https://doi.org/10.1016/B978-0-12-397177-7.00004-8>, 2013.

784 Owusu, P. A. and Asumadu-Sarkodie, S.: A review of renewable energy sources, sustainability  
785 issues and climate change mitigation, *Cogent Eng.*, 3, 1167990,  
786 <https://doi.org/10.1080/23311916.2016.1167990>, 2016.

787 Papachristopoulou, K., Fountoulakis, I., Gkikas, A., Kosmopoulos, P. G., Nastos, P. T., Hatzaki, M.,  
788 and Kazadzis, S.: 15-Year Analysis of Direct Effects of Total and Dust Aerosols in Solar  
789 Radiation/Energy over the Mediterranean Basin, *Remote Sens. (Basel)*, 14, 1535,  
790 <https://doi.org/10.3390/rs14071535>, 2022.

791 Papachristopoulou, K., Fountoulakis, I., Bais, A. F., Psiloglou, B. E., Papadimitriou, N., Raptis, I.-P.,  
792 Kazantidis, A., Kontoes, C., Hatzaki, M., and Kazadzis, S.: Effects of clouds and aerosols on  
793 downwelling surface solar irradiance nowcasting and short-term forecasting, *Atmos. Meas. Tech.*,  
794 17, 1851–1877, <https://doi.org/10.5194/amt-17-1851-2024>, 2024.

795 Paulescu, E. and Blaga, R.: A simple and reliable empirical model with two predictors for estimating  
796 1-minute diffuse fraction, *Solar Energy*, 180, 75–84, <https://doi.org/10.1016/j.solener.2019.01.029>,  
797 2019.

798 Pedro, H. T. C., Inman, R. H., and Coimbra, C. F. M.: Mathematical methods for optimized solar  
799 forecasting, in: *Renewable Energy Forecasting*, Elsevier, 111–152, <https://doi.org/10.1016/B978-0-08-100504-0.00004-4>, 2017.

801 Pfenninger, S. and Staffell, I.: Long-term patterns of European PV output using 30 years of validated  
802 hourly reanalysis and satellite data, *Energy*, 114, 1251–1265,  
803 <https://doi.org/10.1016/j.energy.2016.08.060>, 2016.

804 Qu, Z., Oumbe, A., Blanc, P., Espinar, B., Gesell, G., Gschwind, B., Klüser, L., Lefèvre, M., Saboret,  
805 L., Schroedter-Homscheidt, M., and Wald, L.: Fast radiative transfer parameterisation for assessing  
806 the surface solar irradiance: The Heliosat 4 method, *Meteorologische Zeitschrift*, 26, 33–57,  
807 <https://doi.org/10.1127/metz/2016/0781>, 2017.

808 Raptis, I.-P., Kazadzis, S., Fountoulakis, I., Papachristopoulou, K., Kouklaki, D., Psiloglou, B. E.,  
809 Kazantzidis, A., Benetatos, C., Papadimitriou, N., and Eleftheratos, K.: Evaluation of the Solar  
810 Energy Nowcasting System (SENSE) during a 12-Months Intensive Measurement Campaign in  
811 Athens, Greece, *Energies* (Basel)., 16, 5361, <https://doi.org/10.3390/en16145361>, 2023.

812 Ridley, B., Boland, J., and Lauret, P.: Modelling of diffuse solar fraction with multiple predictors,  
813 *Renew. Energy*, 35, 478–483, <https://doi.org/10.1016/j.renene.2009.07.018>, 2010.

814 Schroedter-Homscheidt, M., Azam, F., Betcke, J., Hanrieder, N., Lefèvre, M., Saboret, L., and Saint-  
815 Drenan, Y. M.: Surface solar irradiation retrieval from MSG/SEVIRI based on APOLLO Next  
816 Generation and HELIOSAT 4 methods, *Meteorologische Zeitschrift*, 31, 455–476,  
817 <https://doi.org/10.1127/metz/2022/1132>, 2022.

818 Shettle, E. P.: Models of aerosols, clouds and precipitation for atmospheric propagation studies,  
819 paper presented at Conference on Atmospheric Propagation in the UV, Visible, IR and MM-Region  
820 and Related System Aspects, NATO Adv. Group for Aerosp, Res. and Dev., Copenhagen, 1989.

821 Stoffel, T.: Terms and Definitions, in: *Solar Energy Forecasting and Resource Assessment*, Elsevier,  
822 1–19, <https://doi.org/10.1016/B978-0-12-397177-7.00001-2>, 2013.

823 Toledano, C., González, R., Fuertes, D., Cuevas, E., Eck, T. F., Kazadzis, S., Kouremeti, N., Gröbner,  
824 J., Goloub, P., Blarel, L., Román, R., Barreto, Á., Berjón, A., Holben, B. N., and Cachorro, V. E.:  
825 Assessment of Sun photometer Langley calibration at the high-elevation sites Mauna Loa and  
826 Izaña, *Atmos. Chem. Phys.*, 18, 14555–14567, <https://doi.org/10.5194/acp-18-14555-2018>, 2018.

827 WMO.: Guide to instruments and methods of observation (WMO-No. 8),  
828 [https://library.wmo.int/doc\\_num.php?explnum\\_id=57838](https://library.wmo.int/doc_num.php?explnum_id=57838) (last access: 1 May 2025), 2021.

829 Yang, D.: SolarData package update v1.1: R functions for easy access of Baseline Surface Radiation  
830 Network (BSRN), Solar Energy, 188, 970–975, <https://doi.org/10.1016/j.solener.2019.05.068>, 2019.

831

832

833

834